



Article

Impact of Dispersive Solvent and Temperature on Supercapacitor Performance of N-Doped Reduced Graphene Oxide

Ankit Yadav ^{1,*}, Rajeev Kumar ^{1,2,*} , Deepu Joseph ³, Nygil Thomas ⁴ , Fei Yan ² and Balaram Sahoo ^{1,*}¹ Materials Research Centre, Indian Institute of Science, Bengaluru 560012, Karnataka, India² Department of Chemistry and Biochemistry, North Carolina Central University, Durham, NC 27707, USA; fyan@nccu.edu³ Department of Physics, Nirmalagiri College, Nirmalagiri, Kuthuparamba, Kannur 670701, Kerala, India; deepuj@nirmalagiricollege.ac.in⁴ Department of Chemistry, Nirmalagiri College, Nirmalagiri, Kuthuparamba, Kannur 670701, Kerala, India; nygill@gmail.com

* Correspondence: ankit.skb02@gmail.com (A.Y.); rkumar@nccu.edu (R.K.); bsahoo@iisc.ac.in (B.S.)

Abstract: This study evaluates the critical roles of the dispersion medium and temperature during the solvothermal synthesis of nitrogen-doped reduced graphene oxide (NG) for enhancing its performance as an active material in supercapacitor electrodes. Using a fixed volume of a solvent (THF, ethanol, acetonitrile, water, N,N-Dimethylformamide, ethylene glycol, or N-Methyl-2-pyrrolidone) as the dispersive medium, a series of samples at different temperatures (60, 75, 95, 120, 150, 180, and 195 °C) are synthesized and investigated. A proper removal of the oxygen moieties from their surface and an optimum number of N-based defects are essential for a better reduction of graphene oxide and better stacking of the NG sheets. The origin of the supercapacitance of NG sheets can be correlated to the inherent properties such as the boiling point, viscosity, dipole moment, and dielectric constant of all the studied solvents, along with the synthesis temperature. Due to the achievement of a suitable synthesis environment, NG synthesized using N,N-Dimethylformamide at 150 °C displays an excellent supercapacitance value of 514 F/g at 0.5 A/g, which is the highest among all our samples and also competitive among several state-of-the-art lightweight carbon materials. Our work not only helps in understanding the origin of the supercapacitance exhibited by graphene-based materials but also tuning them through a suitable choice of synthesis conditions.



Citation: Yadav, A.; Kumar, R.; Joseph, D.; Thomas, N.; Yan, F.; Sahoo, B. Impact of Dispersive Solvent and Temperature on Supercapacitor Performance of N-Doped Reduced Graphene Oxide. *C* **2024**, *10*, 89. <https://doi.org/10.3390/c10040089>

Academic Editor: Olena Okhay

Received: 4 September 2024

Revised: 30 September 2024

Accepted: 8 October 2024

Published: 10 October 2024



Copyright: © 2024 by the authors. Licensee MDPI, Basel, Switzerland. This article is an open access article distributed under the terms and conditions of the Creative Commons Attribution (CC BY) license (<https://creativecommons.org/licenses/by/4.0/>).

Keywords: supercapacitor; reduced graphene oxide; nitrogen doping; synthesis parameters; dispersive solvents

1. Introduction

Graphene, a 2D carbon framework, has attracted marvelous consideration from experimental and theoretical scientific groups in recent times due to its enormous potential for future applications in numerous technological domains, e.g., in the Internet of Things (IoT), batteries, supercapacitors [1], and water splitting [2–4]. The surface and electrical properties of graphene can be tweaked through chemical alteration via heteroatom doping [5–7], which makes N-doped graphene more appropriate for certain applications than pure graphene [8,9]. For instance, N-doped reduced graphene oxide (NG) is used in many applications such as for energy storage devices [10,11], carbon-based biosensing devices with improved biocompatibility [12], etc. Previously, NG sheets were synthesized by the nitrogen plasma treatment of GO at ~300 °C, where precise control on the quality of the rGO is difficult to achieve. Hence, for the synthesis of NG sheets recently, many of the reports employ the hydrothermal/solvothermal method. During hydrothermal synthesis, various nitrogen sources such as dicyanadiazide [13], ammonia [14], glucosamine [15], hexamethylenetetramine [16], pyrrole [17], ammonium oxalate [18], urea [19,20], amino acids [21], and hydrazine [22] are utilized. Similarly, NG sheets are also synthesized by the

solvothermal method using amitrole, urea, or ammonia as a nitrogen source in ethylene glycol or N,N-Dimethylformamide as the solvent [23–25] for their application in energy devices.

For several important electronic and energy device applications, well-dispersed NG sheets are required. However, the preparation of the homogeneously dispersed form of NG sheets is not a straightforward process since its colloidal stability in various solvents at different temperatures is a critical aspect. In this perspective, the dispersibility of graphene oxide (GO)/reduced graphene oxide (rGO) in multiple solvents is examined by several groups [26–28]. The dispersion/quality of the final synthesized NG sheets would depend on the dispersibility of GO, the type of reducing agent, the nature of the particular dispersive solvent used, and the reaction temperature used during the hydrothermal/solvothermal reaction process. However, detailed studies in this regard are lacking in the literature. Furthermore, as usually reported by several researchers, only a minuscule amount of GO (i.e., <1 mg/mL) is usually processed/reduced by the hydrothermal/solvothermal route [24,29,30]. However, for meeting the industrial-scale requirements of high-quality NG, a lacuna of proficient synthesis approaches is explored. These difficulties are mainly due to the contradicting issues of quantity and quality control by the hydrothermal process and other methods, respectively. In achieving such a feat of synthesizing high-quality graphene materials in bulk, the role of various solvents has to be explored, and hydrothermal reaction conditions should be optimized. In this direction, only a few scattered studies are available, but the results cannot be compared due to variability in the parameters. For example, Gopalkrishnan et al. and Jiang et al. studied the hydrothermal/solvothermal synthesis of NG at a few different temperatures but by using only one dispersive solvent [29,30]. Mayyas et al. have studied the in-situ synthesis of NG in different solvent media by the electrochemical method but only at room temperature (RT) [31]. Herein, we intend to explore the critical role of the solvent's intrinsic properties such as the viscosity, boiling point, dielectric constant, and dipole moment, along with the synthesis temperature's effect on the quality of the synthesized NG sheets. Our work not only offers the optimized conditions for the synthesis of large-scale and high-quality NG, but also the mechanistic details governing it. In this study, we aim to investigate how the intrinsic properties of solvents—specifically the viscosity, boiling point, dielectric constant, and dipole moment—impact the quality of synthesized nanoporous graphene sheets. These solvent characteristics can influence key aspects of the synthesis process, including the dispersion of precursors, reaction kinetics, and the overall morphology of the resulting graphenic sheets. Additionally, we will consider how varying the synthesis temperature interacts with these solvent properties to further affect the characteristics of the NG sheets. A more detailed exploration of these relationships will enhance our understanding of optimizing synthesis conditions for improved material quality.

Liu et al. [32] discussed that the high specific capacitance in carbon materials often revolves around their structural characteristics, particularly their porosity and defects. Furthermore, they have some similarities, such as the importance of surface area, the role of surface chemistry, and disorder. Apart from these, the differences are the emphasis on structural disorder, mechanism of capacitance, and the material types and application. In this work, we optimized the synthesis parameters for the hydrothermal/solvothermal reduction of GO by using urea ($\text{NH}_2\text{-CO-NH}_2$) as the reducing agent, which also acts as the nitrogen source for N doping in rGO. For the reduction of GO, i.e., the chemical eradication of oxygen functional groups during the reaction progress, we have used many different (aqueous and organic) solvents to dissolve the reducing agent (urea) and disperse GO and studied the effect of each solvent at different temperatures via the hydrothermal/solvothermal reaction. Urea is chosen as the nitrogen source and reducing agent because it is economical and extensively used by other researchers [20,33]. Based on the effectiveness of the reducing agent in different solvents and the dispersibility of the GO sheets, we explored the plausible reasons behind the variation in supercapacitance behavior exhibited by different samples. In this way, we figure out the optimum conditions favorable

for the large-scale processing of NG, which can meet the demand of the electronic and energy device industries.


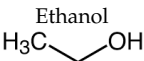
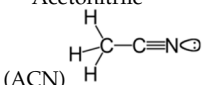
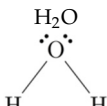
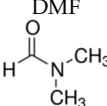
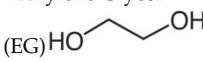
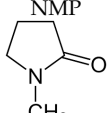
2. Materials and Methods

2.1. Synthesis of GO and N-Doped rGO (NG)

The chemicals used to synthesize graphene oxide (GO) sheets are graphite flake powder purchased from Sigma Aldrich (Bengaluru, India), conc. HCl (35.4%, SD Fine Chemicals Ltd., Mumbai, India), acetone ($\geq 99.5\%$, EMPLURA, Bengaluru, India), KMnO_4 (99%, Qualigens, Mumbai, India), H_2SO_4 (98% GR, MERCK, Bengaluru, India), H_2O_2 (30%, MERCK, Bengaluru, India), and H_3PO_4 (Sigma Aldrich, Bengaluru, India). GO is synthesized using the well-established improved Hummers' method [34,35]. Briefly, 3 g of graphite flakes were taken in a 500 mL beaker and mixed with 360 mL of H_2SO_4 and 40 mL of H_3PO_4 with continuous stirring in an ice bath, and 18 g of KMnO_4 was added to this mixture in small parts. Then, the reaction mixture was allowed to cool to room temperature and washed several times with deionized water, conc. HCl, and ethanol to remove excess acid and oxide impurities. The sample was then dried in an oven at 80°C for 24 h.

The preparatory details and the synthesis procedure for the preparation of NG are given below. For the hydrothermal/solvothermal synthesis of NG sheets, urea was taken as a nitrogen source and dissolved in various solvents. To carry out the hydrothermal/solvothermal synthesis of NG, we used a Teflon-lined autoclave of 100 mL capacity. For the synthesis, 3 g of urea was dissolved in 80 mL of Tetrahydrofuran (THF) solvent, and 1 g of GO was added to this solution. The mixture was then ultrasonicated for 15 min. This ratio of 1:3 for GO/urea and the reaction time of 24 h are chosen according to our earlier work [33], where this combination shows the best supercapacitive performance. The obtained homogeneous mixture was then poured into a 100 mL Teflon-lined stainless-steel autoclave and kept in a muffle furnace at a temperature of 60°C for 24 h for the hydrothermal/solvothermal reduction reaction to occur. After 24 h, when the furnace was cooled down to room temperature, the sample was recovered and washed several times with water and ethanol to remove the organic impurities. The sample was then dried overnight in a hot-air oven at 60°C and labeled as NG-3-THF-60. In a similar way, the N-doped samples were prepared at 120, 150, 180, and 195°C , keeping all other synthesis conditions identical. The samples are correspondingly named NG-3-THF-120, NG-3-THF-150, and NG-3-THF-180, respectively. Similarly, by keeping the same amount of urea and GO (i.e., 3 g of urea and 1 g of GO), the other samples were synthesized by using different dispersive solvents such as ethanol (EtOH), acetonitrile (ACN), water (H_2O), N,N-Dimethylformamide (DMF), ethylene glycol (EG), and N-Methyl-2-pyrrolidone (NMP). The hydrothermal/solvothermal reaction temperatures were chosen between 60°C and 195°C ; in particular, the reaction temperatures of 60, 75, 95, 120, 150, 180, and 195°C were used, depending on the boiling points of the solvents. These selected temperatures range from below the boiling point of all the solvents to that above it. As we will notice later, any temperature below 60°C is not suitable for the removal of oxygen moieties, i.e., the hydrothermal/solvothermal reduction reaction does not occur effectively. Furthermore, there is the danger of damage to the Teflon lining of the autoclave above 200°C . Hence, the temperature range was limited between 60°C and 195°C . Note that our chosen solvents not only have different boiling points but have different viscosities, dipole moments, and dielectric constants too. The details of the solvent properties and corresponding synthesis parameters used, along with the respective sample codes, are listed in Table 1. The details of the characterization methods, including the electrochemical study and the electrode preparation for supercapacitance measurement, are described in the Supplementary Materials (ESI).

Table 1. The physico-chemical parameters associated with different dispersive media used for the synthesis of nitrogen-doped reduced graphene oxide (NG) samples and the corresponding sample codes.

Solvent (80 mL)	Boiling Point (°C)	Viscosity (cP) (25 °C)	Dipole Moment (Debye)	Dielectric Constant	Temp. (°C)	Sample Name
THF 	66	0.48	1.75	7.52	60	NG-3-THF-60
					120	NG-3-THF-120
					150	NG-3-THF-150
					180	NG-3-THF-180
Ethanol 	78.6	0.98	1.69	24	75	NG-3-EtOH-75
					120	NG-3-EtOH-120
					150	NG-3-EtOH-150
					180	NG-3-EtOH-180
Acetonitrile  (ACN)	82	0.33	3.92	36.6	75	NG-3-ACN-75
					120	NG-3-ACN-120
					150	NG-3-ACN-150
					180	NG-3-ACN-180
H ₂ O 	100	0.89	1.85	78.4	95	NG-3-H ₂ O-95
					120	NG-3-H ₂ O-120
					150	NG-3-H ₂ O-150
					180	NG-3-H ₂ O-180
DMF 	153	0.80	3.82	38.25	120	NG-3-DMF-120
					150	NG-3-DMF-150
					180	NG-3-DMF-180
Ethylene Glycol (EG) 	197.6	16.1	2.31	37.7	120	NG-3-EG-120
					150	NG-3-EG-150
					180	NG-3-EG-180
					195	NG-3-EG-195
NMP 	202	1.89	3.75	32	120	NG-3-NMP-120
					150	NG-3-NMP-150
					180	NG-3-NMP-180
					195	NG-3-NMP-195

2.2. Characterization Methods

The X-ray diffraction (XRD) patterns of all our synthesized samples were recorded using a PANalytical X-ray diffractometer X-ray diffractometer (operated at 40 kV and 150 mA) in a 2θ range from 10° to 55° (Cu- K_α radiation, $\lambda = 1.540 \text{ \AA}$). The scanning electron microscopy (SEM) images were obtained through a ‘Supra55 Zeiss’ field emission scanning electron microscope. Raman spectra were taken on ‘LabRam HR’ equipment (with a 532 nm laser source). The X-ray photoelectron spectroscopy (XPS) measurements were performed on an ‘AXIS ULTRA system’. The excitation energy is 1486.7 eV (Al K_α X-ray source), while energy resolution is around 0.5 eV with a monochromated source. The background subtraction was carried out using the Shirley function in Origin software (version 8.1). Spectra fitting was performed manually in Origin software based on the available literature of similar samples.

2.3. Electrochemical Measurements

A potentiostat/galvanostat (Biologic, Model: SP-200, Software: EC-Lab v.11) was employed for all electrochemical experiments. The electrochemical measurements were performed in the three-electrode configuration by using Ag/AgCl (3.5 M KCl) as the reference electrode, a Pt wire as the counter electrode, and 3 mm diameter glassy carbon electrodes (GCEs) as the working electrodes. For exploring the performance of the supercapacitors, cyclic voltammetry (CV), galvanometric charging–discharging (GCD), and electrochemical impedance spectroscopy (EIS) experiments were performed in a 0.5 M H₂SO₄ solution at room temperature (RT) without stirring.

The working electrodes for electrochemical measurements were fabricated using the following procedure: at the start, the glassy carbon electrodes (GCEs), having a surface area of ~0.07 cm², were polished using different grades of alumina slurry (starting from coarse to fine), washed several times with DI water, and dried afterward. Later, by dispersing 2 mg of an as-synthesized powder (e.g., NG-3-THF-60) sample in 500 µL of ethanol through ultrasonication for 15 min, a steady ink-like fluid was prepared. This fluid was then mixed with 2.5 µL of Nafion (5% in isopropanol) as a binder and further sonicated for better dispersion. Afterward, 5 µL of this resulting fluid was drop-cast on a GCE and dried in air (at RT) [8,36]. The dried sample on the GCE works as the working electrode for all the electrochemical experiments. Similarly, using each of the other samples (synthesized by using different solvents at different temperatures), other working electrodes were prepared. Prior to all electrochemical measurements, nitrogen gas was purged onto the electrodes (at room temperature) for removing any accumulated dust on the surface of the working electrode.

From the measured CV curves, the areal capacitance values are obtained through Equation (1) as follows [16]:

$$C_{Areal} = \frac{\int IdV}{A \times v \times \Delta V} \quad (1)$$

where '*I*' denotes the current obtained within a small voltage window *dV* in the CV curve, ΔV represents the total voltage window covering the CV loop, '*v*' is the potential scanning rate, and '*A*' is the surface area of the electrode (~0.07 cm²). The specific capacitance (*C_{sp}*) value (F/g) is calculated from the measured GCD curve by using Equation (2) as follows [37]:

$$C_{sp} = \frac{I \times \Delta t}{m \times \Delta V} \quad (2)$$

here, '*I*' is the implemented constant current (mA), ' Δt ' is discharge time (seconds), '*m*' is the mass (mg) of the sample used on the active electrode surface area, and ' ΔV ' is the difference between the initial and the final potential. Hence, *C_{sp}* is the value of the net specific capacitance (supercapacitance).

3. Results and Discussion

3.1. Morphological and Structural Characterization

3.1.1. SEM Study

The SEM images for two representative samples (NG-3-DMF-150 and NG-3-H₂O-150) are shown in Figure 1. The SEM images of all other samples are given in Figures S1 and S2 (ESI file). It can be seen from the SEM images that the samples appear as sponge-like structures due to the agglomeration/stacking of the interlinked three-dimensional NG sheets, as usually reported in the literature [20]. The strongly packed lamellar and aggregated flaky texture shows the multilayered microstructure of the NG sheets.

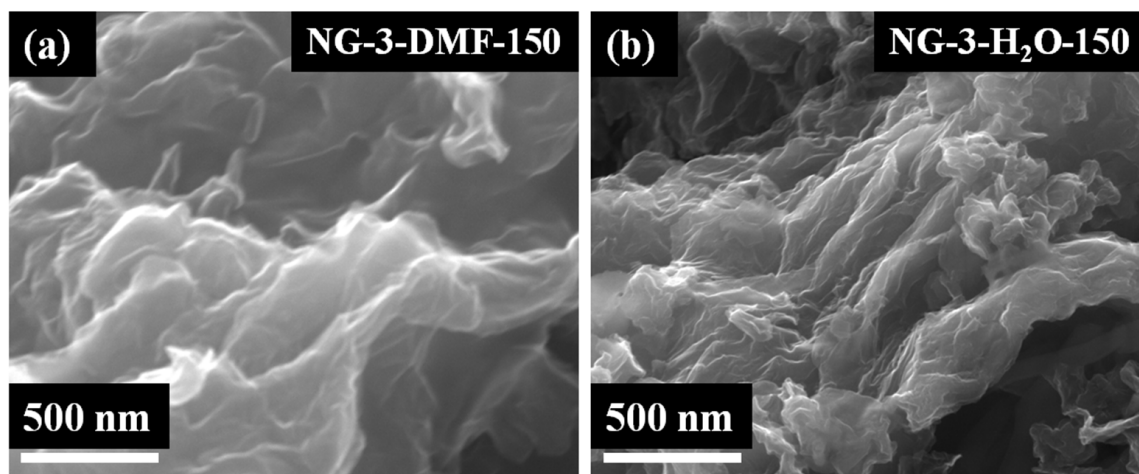


Figure 1. SEM images of (a) NG-3-DMF-150 and (b) NG-3-H₂O-150 samples.

3.1.2. XRD Study

The XRD patterns of all the samples synthesized at different temperatures and by using different solvents are shown in Figure 2. Figure 2a shows the XRD patterns of the synthesized GO and rGO samples. The peak at $2\theta = 10.6^\circ$ for GO represents the (001) Bragg peak associated with an interlayer spacing of about 0.83 nm, whereas the Bragg peak observed at $2\theta = 26^\circ$ for rGO represents the (002) peak associated with an interlayer spacing of 0.34 nm. In carbonaceous materials, both these Bragg peaks are often observed and are indexed as (001) and (002), respectively; hence, we have also indexed them accordingly. These interlayer spacing values are similar to those reported in the literature [24]; however, there is a small variation from report to report due to the concentration and size of different oxygen moieties, viz. -COOH (carboxyl), -C=O (carbonyl), -OH (hydroxyl), -C-O-C- (epoxide), etc. [34], present on the surface of the graphene sheets. Figure 2b shows the XRD patterns of the NG samples synthesized using the THF solvent (NG-3-THF samples) at different temperatures, as indicated. The sample synthesized at the lowest temperature (60°C) shows the prominent peak at $2\theta = 10.6^\circ$ corresponding to the (001) diffraction peak of GO, along with a broad hump at $2\theta \approx 26^\circ$. This proves that GO is not completely reduced, but some oxygen-containing functional groups are still present on the basal planes. At higher temperatures, i.e., $\geq 120^\circ\text{C}$, the (001) peak at $2\theta = 10.6^\circ$ for GO disappears from the XRD patterns, and the sharp peak corresponding to the (002) Bragg peak of rGO appears at $2\theta \approx 26^\circ$. This illustrates that the oxygen moieties are removed from the surface of the GO sheets, which leads to lower interplanar spacing and the formation of the reduced graphene sheets that stack on each other, forming multilayers. As seen from Figure 2b, as the hydrothermal reaction temperature increases from 120°C to 150°C , the (002) Bragg peak (corresponding to the graphitic-type arrangement of the sheets) shifts toward higher 2θ values, indicating that the stacking of the graphenic sheets becomes better, i.e., the crystallinity improved. However, as the hydrothermal reaction temperature increases to 180°C , a broad peak/shoulder emerges at $2\theta \approx 21^\circ$, and the graphitic peak also becomes broad. The appearance of these broad peaks in the XRD patterns indicates lower ordering due to the breakage of the graphenic network. Hence, the high solvothermal reaction temperature of 180°C is unfavorable/unsuitable for the stability of the graphenic sheets during their synthesis when using low-boiling solvents such as THF.

The other sets of samples synthesized using different solvents also show similar features in the XRD patterns (Figure 2), as explained above. However, the temperatures at which these features are observed vary depending on the other synthesis conditions for the different sets of samples. Overall, as the reaction temperature increases above $\sim 60^\circ\text{C}$, there is a gradual sharpening of the (002) XRD peak of the samples synthesized using the reaction temperatures of up to a certain value, and beyond that reaction temperature, this

peak gradually becomes broad. This can be rationalized by inspecting the XRD patterns of all the samples synthesized at different temperatures by using different dispersive media.

From the above discussion, it seems that the choice of the hydro/solvothermal reaction temperature in relation to the boiling point of the solvents may be important. One can rationalize that if the synthesis temperature is below the boiling point of the solvents, the GO is not reduced properly. From Figure 2a–e, it appears that if the reaction temperature is below the boiling point of the solvent, the GO is only partially reduced. Moreover, for the hydro/solvothermal reaction temperature of $\sim 95^\circ\text{C}$ (which is below the boiling point of water), although no GO peak is observed (Figure 2e), the partial reduction of GO is evident due to lower 2θ positions of the observed broad peaks (i.e., higher interlayer spacing caused due to the presence of some of the oxygen moieties). This discards the relationship between the boiling point and the hydro/solvothermal reaction temperature for the reduction of GO. Furthermore, it is known in the literature that the thermal reduction of GO (to form rGO) occurs at $\sim 110^\circ\text{C}$ or lower at ambient (open furnace) conditions [38]. In case of both EG and NMP, whose boiling points are above 195°C (Table 1), all the chosen synthesis temperatures (for these solvents) are below the boiling points of EG and NMP. This further supports our observation that the boiling point has very little role in controlling the reduction of GO. However, our observation of the partial reduction of GO even at reaction temperatures $\leq 95^\circ\text{C}$ (Figure 2a–e) suggests that the solvents in the hydro/solvothermal method help in the better dispersion of GO and also in lowering the reaction temperature to $\leq 95^\circ\text{C}$ due to this better dispersion.

Closely observing the gradual sharpening of the (002) Bragg peaks for samples synthesized at different temperatures and different solvents, we can understand that the stacking of the NG sheets becomes better at different temperatures for the various solvents. This provides us with better insights into choosing a suitable solvent and optimizing the synthesis temperature for improving the functional behavior of the NG. Since there is an incomplete reduction of GO for the samples synthesized below 95°C (i.e., NG-3-THF-60, NG-3-EtOH-75, and NG-3-ACN-75 samples), we have excluded these samples from further analysis. Furthermore, from Figure 2, we have observed high disorderliness in the NG samples (emergence of a broad shoulder at $2\theta \approx 21^\circ$ along with broadening of the (002) peak) for all the different sets of samples synthesized using different solvents above $\sim 180^\circ\text{C}$. Hence, combining all the above discussion, we can understand that if the synthesis temperature is below $\sim 95^\circ\text{C}$, an incomplete reduction of GO occurs, while for temperatures above $\sim 180^\circ\text{C}$, the heavily disordered NG flakes are obtained. Hence, our investigations provide us a synthesis temperature window between 120 and 180°C , which can be further optimized for obtaining perfect NG sheets with optimized supercapacitor performance.

The analysis of the supercapacitance behavior of our NG samples will be demonstrated later, but understanding the origin and optimization of supercapacitance performance shown by our NG samples is the goal of the present study. To obtain detailed insights into the origin and mechanism of the supercapacitive behavior of our synthesized samples, the structural details and the nature of stacking of the NG sheets are very important. Hence, we have least squares fitted the (002) Bragg peak of each of the NG samples and calculated their crystallite sizes (L_c) through the Debye–Scherrer equation (Equation (S3), ESI). These crystallite sizes essentially define the thickness of the NG flakes over which the stacking is proper. The broad peak present at $2\theta \approx 26^\circ$ for all the samples is fitted with two sub-peaks (as given in Figures S3 and S4 (ESI)), where the subpeaks seen at lower angles ($\sim 21.3^\circ$, assumed as peak 1) and at higher angles ($\sim 25.7^\circ$, assumed as peak 2) correspond to the amorphous/disordered and graphitic-type/crystalline arrangement of the NG sheets, respectively. The detailed results of the least squares fitting of the (002) Bragg peaks for all our samples are listed in Table S1 (ESI).

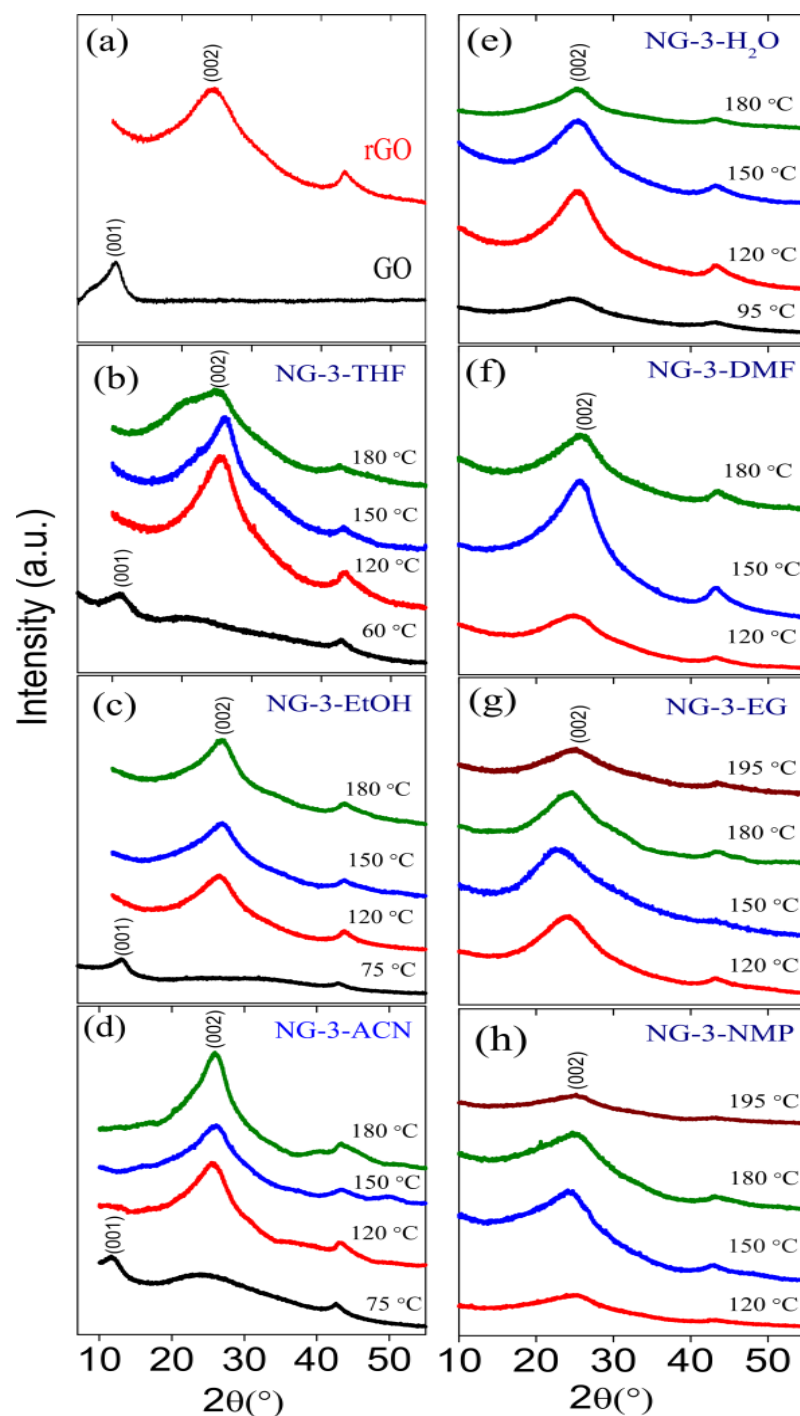


Figure 2. The XRD pattern of the (a) GO and rGO, and (b–h) NG-3 samples synthesized in various dispersive media and at different temperatures, as indicated.

From Table S1, it is clear that for the NG samples synthesized using THF, EtOH, ACN, water, DMF, EG, and NMP as the solvent, the best crystallinity is obtained either at 150 or 180 °C, respectively. As discussed above, the boiling point is not a very important parameter for the hydro/solvothermal reduction of GO. However, as a variation in the degree of crystallinity is observed at different reaction temperatures for the various dispersive solvents, it indicates that other inherent physical properties of the solvents such as the viscosity, dielectric constant, dipole moment, etc., can be important in this respect [39–41]. As these physical properties of the solvents depend on the temperature, the boiling point plays its role in controlling the nature of stacking/structural aspects of NG during their

synthesis. For example, a low dielectric constant of the solvent may not facilitate improved activity of the NH_3 and CO/CO_2 molecules (originating from the reducing agent, urea) and as a result, the proper reduction of GO or proper dissociation of the oxygen moieties from the surface of GO does not occur. In addition, another important inherent property that may control the reduction of GO is the dipole moment of the solvent. If the solvent molecules have a high dipole moment, i.e., if the solvent is highly polar, they will facilitate better interaction with the oxygen moieties and other polar groups present on the basal plane of GO. This better GO sheet–solvent interaction can immensely help in the reduction of GO. Furthermore, a low viscosity of the solvent provides better dispersibility to GO and improves the mobility of the NH_3 and CO/CO_2 molecules present in the fluid, which helps in a better reduction of GO (along with better N doping in the basal carbon plane of the graphenic sheets). Simultaneously, a better reduction and suitable dispersibility help in a better stacking of the reduced GO sheets, which in turn decides the crystallinity of the NG flakes. The role of all the solvent parameters in controlling the structural and electrochemical aspects of the synthesized NG flakes is further explored.

3.1.3. Raman Spectroscopy Study

For examining the amount of surface defects and the nature of the disorder in the NG samples, we have performed Raman spectroscopy. As expected, each of the Raman spectra consists of two broad peaks positioned at the Raman shifts of ~ 1342 and $\sim 1583\text{ cm}^{-1}$, which are known as the disorder (D) and the graphitic (G) peaks, respectively. The relative amount of surface defects of the samples can be determined by the integrated intensity ratio of the G and the D peaks [35]. However, for an accurate determination of the amount and the type of defects present in each sample, we have performed a rigorous analysis of the fitting results. For this, each Raman spectrum is fitted with five sub-peaks (Figure S5) by using Gaussian–Lorentzian functions. Detailed explanations are given in Section 3.2 (ESI).

In our previous study, we have discussed the detailed analyses of Raman spectra of GO and rGO and evaluated the number of layers, which are 9.1 and 12.5, respectively [33]. From Table S3 (ESI), it is clear that the intensity of the D3 peak (which corresponds to the amorphous-type defects) for the samples prepared using a particular solvent (at different temperatures) varies in a similar trend as that observed for the amorphous carbon peak (peak 1) of the XRD patterns (Table S1). This relationship is also valid for the variation in the area under the G-peak of the Raman spectra and the crystalline graphitic peak (peak 2) of the XRD patterns of the corresponding samples prepared using a particular solvent. Notably, the D3 peak intensity is the lowest, and the G-peak intensity is the highest for the samples prepared at $150\text{ }^\circ\text{C}$ (THF), $180\text{ }^\circ\text{C}$ (EtOH), $180\text{ }^\circ\text{C}$ (ACN), $150\text{ }^\circ\text{C}$ (water), $150\text{ }^\circ\text{C}$ (DMF), $180\text{ }^\circ\text{C}$ (EG), and $180\text{ }^\circ\text{C}$ (NMP) temperatures for the corresponding solvents given within brackets. This is also observed in the XRD patterns of the amorphous carbon peak (having a low intensity) and the graphitic peaks (having a high intensity) for the samples prepared at the same temperatures and by using the same solvents, as given above. Note that the crystallite size obtained using Scherrer's formula through the XRD linewidth (FWHM) corresponds to the thickness perpendicular to the plane, or the '*out-of-plane thickness*' of the graphene sheets of the graphitic flakes, whereas the crystallite sizes obtained using the Tuinstra–Koenig formula (Equation (S4)) through the I_G/I_D intensity ratios of Raman spectra correspond to the '*in-plane thickness*' of the graphene sheets present in the flakes. This is because the Raman spectrum sees only the vibrational modes associated with the bonds in the plane of the graphene sheet, and the graphene sheets are not bonded (no covalent bond) with the neighboring graphene sheets in the flakes. Hence, by combining the results from the XRD and Raman spectra, i.e., both the in-plane and out-of-plane crystallite size, one can rationalize the overall size of the nano-graphite crystallites. From our results, it is clear that the nano-graphite crystallites are bigger in size and better in quality for the sample prepared at an optimum temperature in a particular solvent. Depending on the nature of the solvent and synthesis temperature, the thickness of the nano-graphite crystallites varies from $\sim 1.5\text{ nm}$ to $\sim 2.2\text{ nm}$ (Table S1, ESI), and the in-plane sizes vary

from ~2 nm to 4 nm (Table S4, ESI). Hence, our Raman study emphasizes the role of the hydro/solvothermal reaction temperature and the dispersive solvents in controlling the size and crystalline quality of the synthesized NG flakes.

3.2. Electrochemical Properties

The electrochemical techniques, such as cyclic voltammetry (CV), galvanostatic charge-discharge (GCD), and electrochemical impedance spectroscopy (EIS), were used to estimate the electrochemical performance of our NG samples. As given earlier, the NG samples were used as the working electrode in a three-electrode configuration of the measurement system. We have used 0.5 M of a H_2SO_4 aqueous electrolyte and recorded the electrochemical results in a voltage range between 0 and 0.8 V, which is the selected non-Faradic region. Figure 3 shows the CV voltammograms recorded at a scan rate of 5 mV/s for the NG samples prepared using different solvents and at various temperatures, as indicated. It can be seen that all the voltammograms have almost rectangular shapes with symmetrical current-potential characteristics. This suggests that the supercapacitance is originating due to the electrochemical double layer (EDL) formation, but not through the occurrence of any electrochemical redox reaction.

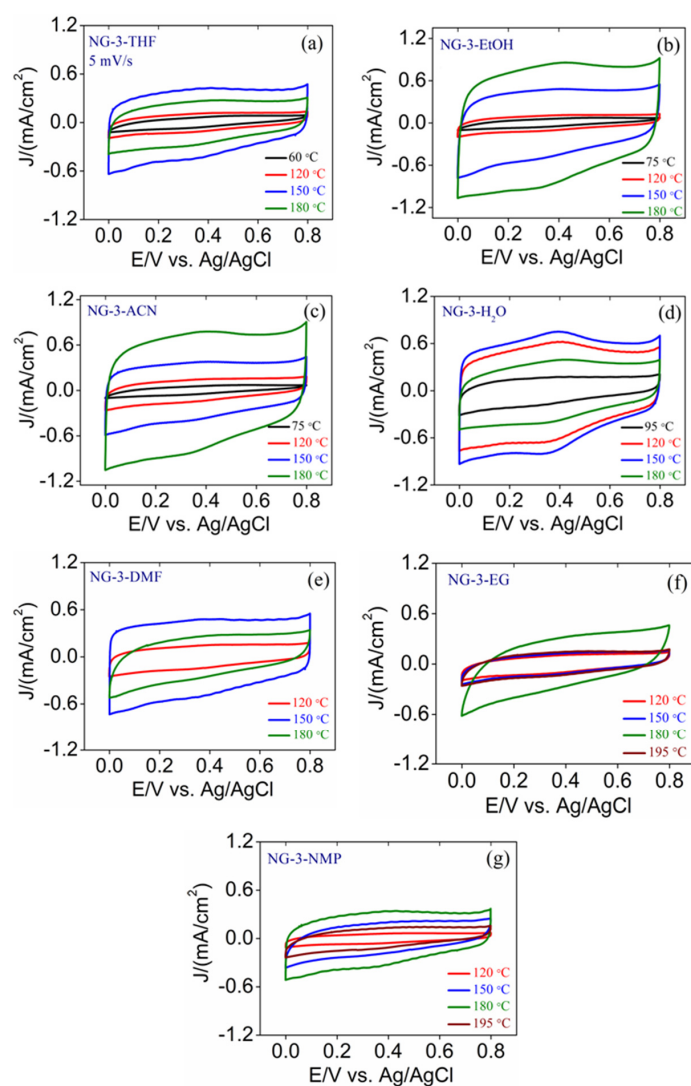


Figure 3. (a) Cyclic voltammograms of all the NG samples at different temperatures with various dispersive solvents, measured at a fixed scan rate of 5 mV/s. The solvents used for synthesis are (a) THF, (b) ethanol, (c) acetonitrile, (d) H_2O , (e) DMF, (f) ethylene glycol, and (g) NMP.

The areal capacitance values of our samples are calculated from the measured CV by using Equation (1). The obtained capacitance values are given in Table 2. It is clear from Figure 3 and Table 2 that the measured capacitance values obtained for the samples prepared using a particular solvent at different synthesis temperatures vary. Furthermore, when comparing the CV curves for the samples prepared using different solvents but at a particular temperature (with all the other experimental conditions being the same), we find variations in their features.

Table 2. The areal capacitance (C_{Areal}) calculated using the CV curves and the specific capacitance (C_{sp}) calculated using discharging of the GCD curves for our NG samples synthesized using different solvents.

Solvent	Temp (°C)	C_{areal} (mF/cm ²)	C_{sp} (F/g)
THF	60	6.38	22.28
	120	16.33	58.31
	150	72.70	259.35
	180	45.77	164.48
Ethanol	75	5.44	19.55
	120	16.88	60.82
	150	69.42	249.82
	180	75.53	268.88
Acetonitrile	75	4.79	19.05
	120	28.57	101.12
	150	51.23	185
	180	75.26	270.58
H ₂ O	95	35.72	102.64
	120	91.03	327.58
	150	103.44	371.87
	180	67.58	241.03
DMF	120	24.49	85.78
	150	141.60	513.86
	180	64.10	234.7
Ethylene Glycol	120	16.49	59.36
	150	21.13	76.08
	180	58.98	208.85
	195	23.25	83.85
NMP	120	8.60	30.32
	150	33.56	119.92
	180	59.76	214.03
	195	19.44	68.27

For example, consider all the NG samples prepared using THF as the solvent (Figure 3a). As the synthesis temperature increases from 60 °C to up to 150 °C, the current density gradually increases, but with a further increase in the synthesis temperature to 180 °C, the current density decreases. This behavior suggests that the conductivity and mobility of the charge carriers, especially in the carbonaceous layer, changes accordingly, as discussed below. This change can only be associated with the size and quality of crystallinity of the nano-graphitic regions in the sample. According to the XRD and Raman spectroscopy results (Tables S1 and S4, ESI), the nano-graphite crystallites become bigger in size and better in crystallinity as the synthesis temperature increases up to 150 °C (for the THF solvent) and it decreases beyond 150 °C. Hence, the nano-graphitic regions in the flakes have better crystallinity and are bigger in size for the sample prepared using THF as the solvent at 150 °C as compared to the other samples prepared at lower or higher synthesis temperatures. As the graphitic regions are better conductors than the amorphous carbon regions, the higher current density in the NG-3-THF-150 sample is justified.

Now, comparing the variation in current density for the samples prepared with different solvents (Figure 3), we observe that the sample synthesized using H₂O as the solvent has the highest current density (and the CV loops have the highest area), and the

sample synthesized using EG has the lowest current density (and the loops have the lowest area). This low current density (or conductivity) of the samples prepared by EG depicts its more insulating character. This higher insulating character of the samples can originate due to the incomplete removal of the oxygen moieties from the surface of the samples (low reduction of GO), where the surface oxygen moieties block the charge transfer behavior. This aspect is further explored through the analysis of the XPS results, as discussed later.

Carefully inspecting all the CV curves (Figure 3), we realize that the CV curves for some of the samples have small redox peaks, which is an indication that these samples have a tendency for redox reactions. The redox peaks are prominent for the samples showing high current densities, i.e., for the samples synthesized using EtOH, ACN, and H₂O as solvents. This high current density in combination with the redox peaks for these samples suggests that the surface of these samples facilitates better charge accumulation and also the tendency to react with the charged species. In general, an ideally flat graphene surface, having no defects, is not prone to react with the accumulated charge species (hence, they show perfect EDLC behavior) [42]. Thus, the tendency for a redox reaction to occur for these samples indicates that the surface of these NG sheets has more defects than the samples where the redox peaks are not prominent. This aspect of the samples can be verified by comparing the XRD patterns of the samples synthesized using different solvents (at the optimum temperatures), especially by referring to the (002) XRD peaks (Figure 1). The samples synthesized using EtOH (at 180 °C), ACN (at 180 °C), and H₂O (at 150 °C) as solvents have broad (002) peaks (due to the presence of the pronounced amorphous shoulder to the left) as compared to that of the samples prepared using DMF (at 150 °C), THF (at 150 °C), NMP (at 180 °C), and EG (at 180 °C) as solvents. This clearly proves that the samples prepared using EtOH (at 180 °C), ACN (at 180 °C), and H₂O (at 150 °C) as dispersive solvents have a higher amount of surface defects. These defects create energy levels within the electronic bandgap, which leads to higher conductivity and a high current density for these samples, as observed.

From the above discussions, it can be inferred that the various solvents facilitate the reducing species (NH₃ and CO/CO₂ present in the solvent) differently to reach the site of the oxygen moieties of GO, thereby reducing it. This leads to the modification in the structural aspects of the NG sheets and in turn, the supercapacitance of the samples. Note that although the FWHM of the XRD (002) peak of the samples prepared at the lower (than the optimum) temperatures are higher, they do not show a prominent redox peak. This is because the higher peak width for the low-temperature synthesized samples is not due to the presence of the higher number of defects, but rather due to the improper reduction of the GO sheets, as discussed earlier (effect of temperature). These oxygen moieties act as a shield for the redox reaction. Hence, these samples show a lower current density and lower capacitance (Figure 3 and Table 2).

From Table 2, it is clear that the sample prepared using DMF shows the highest 'areal' and 'specific' capacitance, followed by those of the samples synthesized using H₂O and ACN. These samples demonstrate better reduced (bare, without having much oxygen moieties) surfaces of the NG sheets with higher number of defects. As there are more defects, it seems they allow the diffusion of charged species (from the solution) at the surface of the sample, originating as the oxidation peak in the CV curves.

Figure 4 shows the galvanostatic charging–discharging (GCD) curves for all our synthesized samples. In the CV curves (Figure 3), we observed a constant current density over the potential range of 0 to 0.8 V, and the same potential range is covered here in the GCD curves, i.e., all the samples are charged to a voltage of 0.8 V by application of a constant current density of 0.5 A/g. Note that the mass of the sample (electrode material) is estimated during the preparation of the electrodes. All the plots exhibit nearly linear discharge–time profiles, revealing an exemplary capacitive behavior. Generally, in all the GCD curves, four different features can be noticed, namely (1) the initial fast charging, (2) forced (slow) charging by the applied current up to 0.8 V, (3) fast discharging (also known as IR drop), and (4) slow discharging to 0 V. The fast charging and fast discharging

occur through the highly mobile charged species, mostly by the electrons transiting to the conduction band (because the motion of the ions in the electrolyte is slow to make this IR drop). Here, 'I' corresponds to the electronic current and 'R' represents the resistance offered by the material to these electrons' motion. As soon as a small current is applied, these highly mobile charges (electrons) accumulate and increase the voltage (charging). Similarly, during the discharging experiment, these electrons move out rapidly and initially discharge the capacitor very fast, known as IR drop. This occurs as soon as the applied current is removed and the capacitor is allowed to discharge. As these electrons do not originate from the electrolyte or from the ions in the electrolyte, they have their origin in the electrode material (i.e., our NG sample). It is known that the structural defects in the carbonaceous materials create electronic defect levels within the energy bandgap of the materials. Depending on the concentration of these defect levels, the conductivity of the carbonaceous materials change. These defect energy levels (within the bandgap) facilitate the electrons to transit to the conduction band through hopping, requiring only a small voltage to be created within the material and pass current. Ideally, for materials having no defects, there will be no conduction until a voltage equivalent to the band gap energy is provided. However, the presence of too many of the defects in the materials (as in the case of amorphous-type materials), the electrical resistivity is enhanced through the scattering of the electrons by the defects in their path during transport.

Hence, often a moderate number of defects in the carbonaceous materials helps in obtaining better conductivity. As we have observed in the XRD patterns, when the FWHM of the (002) peak is high or has a shoulder, it signifies that a different degree of disorder exists in the samples synthesized through different solvents. These results were further supported by the results from the Raman spectroscopy study. Hence, we can understand the GCD curves through the structural and associated electronic properties of the carbonaceous (NG) materials used.

Followed by the initial fast charging and the IR drop region of the GCD curves, the slow charging and discharging region is observed. The origin of this slow charging/discharging behavior is basically governed by the diffusion/hopping-mediated motion of the charged species. Unlike the fast charging or IR drop region (where electrons are the only charge carriers), the charge carriers during this slow charging/discharging process are both electrons and ions. This includes the diffusion of electrons through the electronic defect levels and the ions diffusing into the electrode material and within the electrolyte. As we have used aq. H_2SO_4 (0.5 M) as the electrolyte during the GCD measurements, the ions present in the electrolyte are H^+ and SO_4^{2-} . Considering the faster dynamics of the ions in the solution than that of diffusion into the electrode material, we may further divide the slow charging/discharging regions of the GCD curves into two different regions. The regions that immediately follow the fast-charging region can be assigned to the diffusion of electrons inside the electrode materials and the arrangement of the ions in the electrolyte to form the double layer near the electrode surface. The opposite process happens in the region following the IR drop regions. Furthermore, the last (very slow) part of the charging and discharging curves can be assigned to the diffusion of only the ions into or out of the electrode material, respectively.

Let us understand the GCD curves obtained for different sets of samples prepared using different solvents and at different temperatures (Figure 4). Consider first the charging time observed for a set of samples prepared at different temperatures using a particular solvent; for instance, let us analyze Figure 4d. Here, we observe that as the hydrothermal synthesis temperature increases up to 150 °C, the time taken by the samples for fully charging the capacitor (up to 0.8 V) gradually increases from 256 s to 855 s (these values are obtained for the sample synthesized at 95 °C and 150 °C, respectively), whereas it decreases to 559 s for the sample synthesized at a higher temperature, 180 °C. This observation confirms that for the samples having bigger sized and high-quality nano-graphitic crystalline regions (observed from XRD and Raman spectroscopy), it takes a longer charging time to reach 0.8 V, whereas this charging time decreases for the samples synthesized at a higher

temperature than the optimum temperature. This behavior is universally observed in all different sets of samples (prepared using different solvents), as seen in Figure 4.

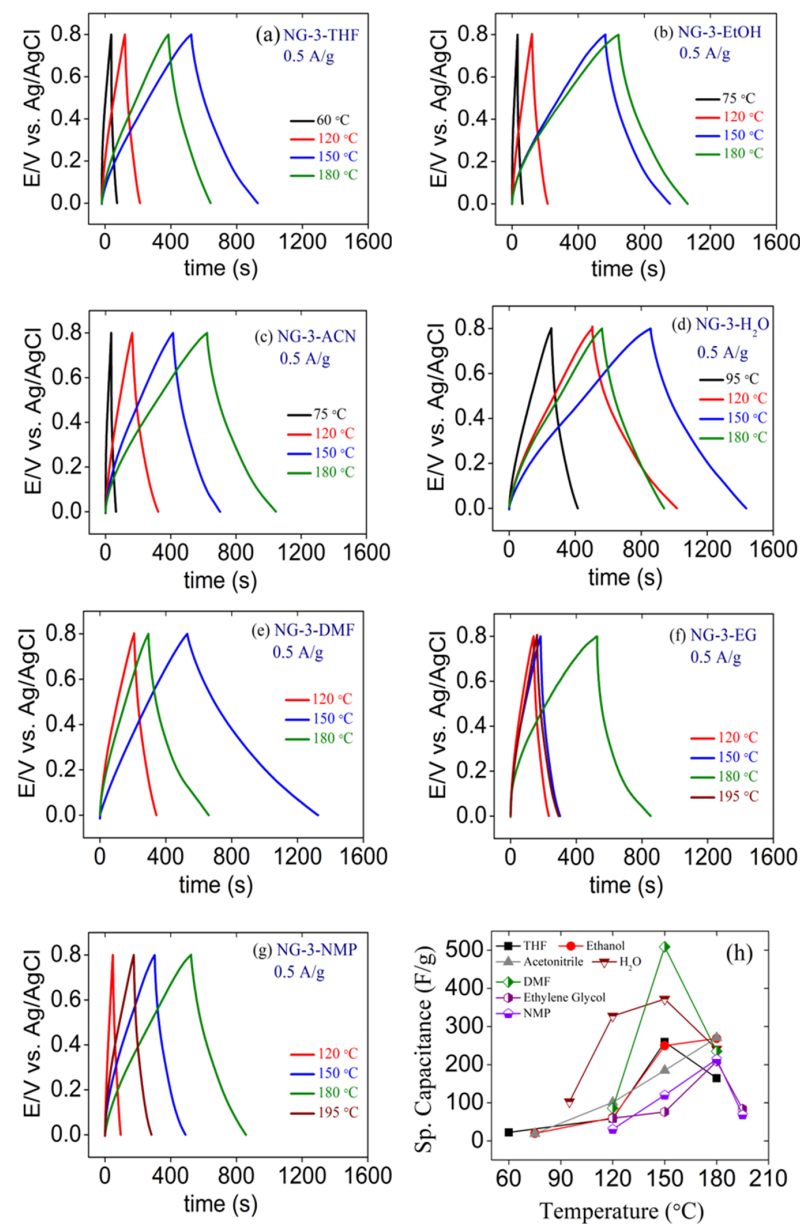


Figure 4. (a) The galvanostatic charging–discharging (GCD) plots for all the NG samples synthesized at different temperatures with various dispersive solvents as indicated. (a) THF, (b) ethanol, (c) acetonitrile, (d) H₂O, (e) DMF, (f) ethylene glycol, and (g) NMP. (h) The specific capacitance of all the NG samples is calculated from the discharging region of the GCD curves by using Equation (2).

As discussed earlier, for any temperature below the optimum synthesis temperature, an improper reduction of GO occurs, and the oxygen moieties (that still remain on the sheets) do not facilitate better stacking of the NG sheets. Furthermore, the presence of more oxygen moieties on the surface of the graphene sheets makes the graphene sheet more insulating, and they do not permeate the ions of the electrolytes to diffuse into the electrode material, as they act as a shield against the charge intercalation/accumulation in the electrode materials. However, for any synthesis temperature above the optimum temperature, the creation of too many defects is observed by XRD and Raman spectroscopy. This reveals the voids created in the graphene sheets due to the high-temperature synthesis of the sample, and the presence of voids in the graphene sheets makes the graphitic flakes

amorphous-like. This leads to a slow permeation of the ions (present in the electrolyte) into the electrode material through these voids. The opposite process occurs during the discharging experiments. Hence, the oxygen moieties are key in providing the insulating and impermeable (to foreign ions) nature of the samples, thereby controlling the overall nature of the GCD curves. This aspect will be further explored in the XPS results.

The fast charging and discharging observed in the GCD curves for the sample prepared at low temperatures (lower than the optimum temperature) could be assigned to the fast formation/dispersion of the double layer by the ions in the electrolyte. As these samples do not conduct electronically and the ions in the electrolyte are shielded by the oxygen moieties to become intercalated in the NG sheets, they facilitate the formation of double layers. The GCD curves of the samples prepared using EG as the solvent clearly reveal this aspect. Furthermore, this aspect of the samples can also be rationalized from the CV curves (Figure 3), where these samples show better EDLC behavior than the samples prepared at the optimum temperature. Hence, as discussed in the previous paragraph, the origin of the gradually increasing charging time with an increase in the synthesis temperature of the samples (up to the optimum synthesis temperature) is due to the facilitation/permeation for the ion diffusion or electron diffusion into the graphitic flakes. With any further increase in the synthesis temperature above the optimum temperature, the amorphous-type graphitic flakes do not offer the slow motion of the ions of the electrolytes; hence, the charging and discharging time decreases again. This understanding can be universally applicable to all our samples.

When we compare the GCD curves among the samples prepared using different dispersive solvents, another interesting point to note is the difference in the charging and discharging times. A low charging time saves time by quickly charging the device, while slow discharging saves energy by decreasing leakage; hence, a better supercapacitor should have a low charging time and long discharging time. As stated earlier, the (002) XRD peak for the sample prepared by using DMF as the solvent (at 150 °C) is the sharpest among all samples, and the quality of crystallinity observed by Raman spectroscopy for this sample is the highest. This suggests that an optimum number of defects, suitable for slow discharging, is created for this sample at the given synthesis condition (i.e., at 150 °C by using DMF). This is the most plausible explanation for the long discharging time or slow diffusion during the discharging of the sample. This suggests that the choice of the dispersive solvent and the synthesis temperature are the most important parameters in obtaining high-quality NG samples for energy storage applications, such as supercapacitors.

As the discharging time is more important for the application of the device and to store energy for a long time, we have calculated the specific capacitance (C_{sp}) for all our samples through Equation (2) by taking the discharging curve into account. The obtained specific capacitance values are provided in Table 2. It is seen that among all the samples synthesized at different temperatures and in different dispersive solvents, the sample synthesized at 150 °C by using DMF as the dispersive solvent shows the highest C_{sp} value of 514 F/g (at a 0.5 A/g current density). To further explore the behavior of the samples, we have measured the CV curves at different scan rates, as shown in Figure S7(a,c,e) (ESI file). From these CV curves, it can be rationalized that as the scan rate increases from 5 mV/s to 100 mV/s, the rectangular nature of the CV curves decreases. This reveals that the diffusion time scales for the charged species are different due to the nature (activity) and the type of defects present on the surface of the NG sheets being different, and they interact differently with the charge's species. To further explore the nature of the samples, we have measured the GCD curves at different current densities, as shown in Figure S7b,d,f. As the current density increases, the charging and discharging time of our NG-based capacitors decreases. It can be understood that the ions quickly charge and discharge the capacitors, similar to that observed in the case of the CV curves.

To understand the variation in the supercapacitance values obtained for our samples and to support the XRD, Raman spectroscopy, CV, and GCD results given earlier, electrochemical impedance spectroscopy (EIS) studies were performed for all our samples

in the range of frequency between 100 mHz and 200 kHz with a sine wave amplitude of 5 mV. Figure 5 demonstrates the Nyquist plots (the imaginary (Z'') versus real (Z') part of the impedance, Z^*) for all our NG samples. These plots can be broadly categorized into two regions, (1) the high-frequency (semicircular) region (near the origin) and (2) the low-frequency (linear/Warburg) region. In all the impedance plots, we observe a (not well-pronounced) semicircular region in the high-frequency part and a nearly straight line in the low-frequency part of the Nyquist plots.

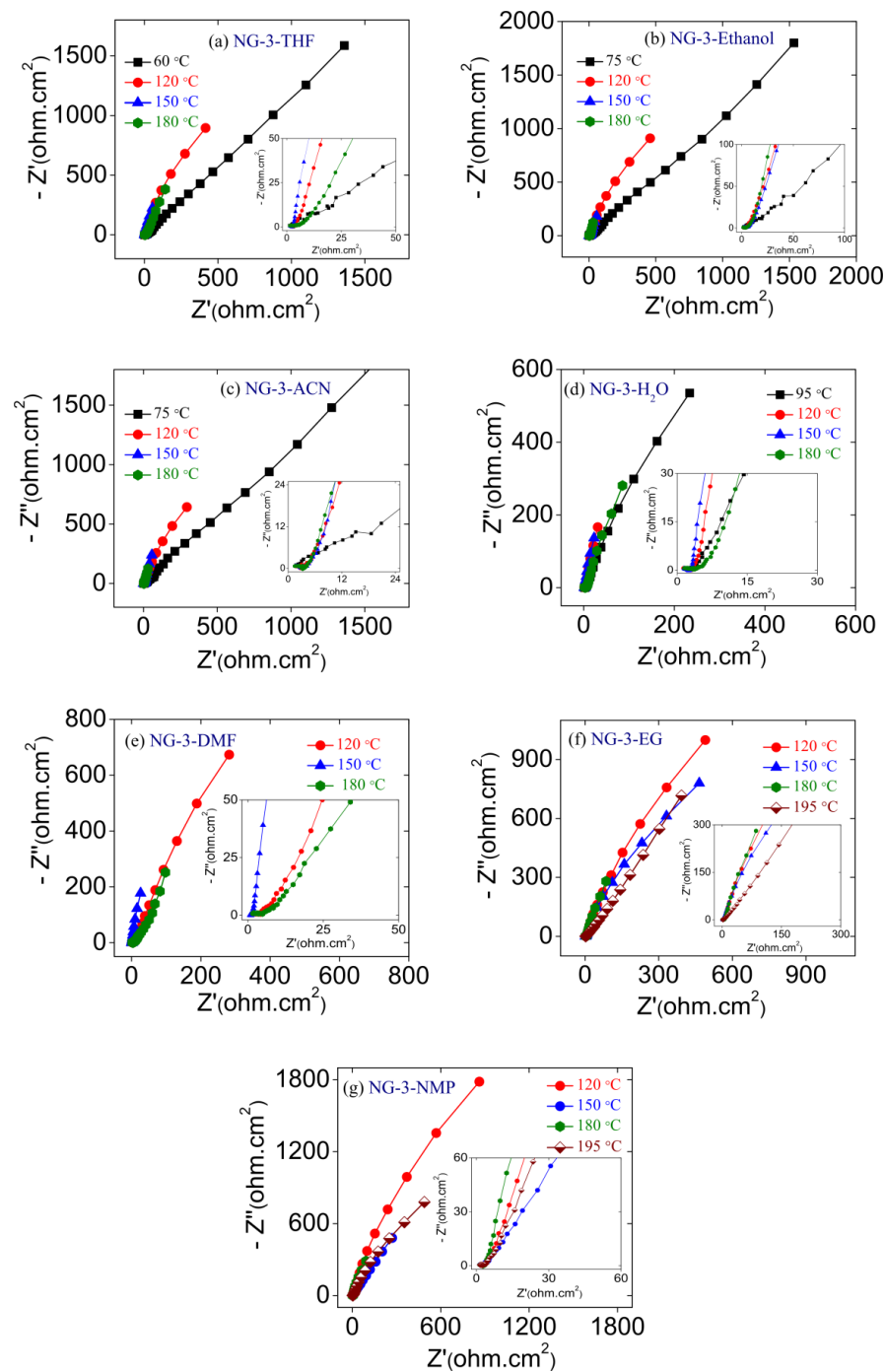


Figure 5. EIS spectra of all our synthesized NG samples at different temperatures in various dispersive solvents.

In general, the presence of semicircles in the high-frequency region is related to the electronic response within the electrode materials and also the electronic charge transfer

into or out of the electrode material through diffusion. The value at which the semicircular region (if extended) would cut the Z' axis is the charge transfer resistance (R_{ct}). This charge transfer can be the electronic transport within the NG materials or the diffusion of the ions into the NG materials. The higher the value of R_{ct} , the more difficult it is for the charge transfer. In our NG materials, this could happen in the following two situations: (1) if the NG material on the electrode is more resistive to electronic motion, i.e., if the crystallinity of the graphitic flakes becomes too poor and/or the presence of a high amount of oxygen moieties, which offers an insulating character to the NG sheets, and (2) if the ions in the electrolyte are not allowed to diffuse into the electrode material, i.e., if the NG sheets are not properly reduced (the amount of the oxygen moieties is still greater on the surface, which repels the ions). The low-frequency linear (straight-up) region shows the characteristics of the ion accumulation at the surface of the materials and forms the EDL, i.e., the ions in the electrolyte forms the double layer at the electrode–electrolyte interface [43,44]. It is clear that if the low-frequency linear region is parallel to the y -axis ($-Z''$), it signifies the formation of a perfect EDL capacitor at the interface, whereas a decrease in the slope of this linear region occurs due to the diffusion of ions from the first ionic layer into the electrode material. Furthermore, the highest (top) value of this part (at a certain low frequency) is the maximum capacitance contributed by the ions, including EDL and diffusion behavior.

In all the sets of samples prepared in different solvents, it can be rationalized that the samples prepared at the lowest temperatures show the highest R_{ct} (Figure 5 (insets)). This suggests that these NG samples have a more insulating character due to the improper reduction of GO, leading to the presence of the oxygen moieties on the NG sheets, as discussed earlier. It can also be rationalized that for the samples prepared at the optimum temperatures, the low-frequency linear (tail) region has the highest slope (Figure 5) among the set of samples prepared using a particular solvent, i.e., at 150 °C (THF), 180 °C (EtOH), 180 °C (ACN), 150 °C (water), 150 °C (DMF), 180 °C (EG), and 180 °C (NMP) temperatures for the solvents mentioned inside the brackets. This suggests that these samples have a better flat surface and perfect EDL formation, which contributes more to the net capacitance of the samples. This can also be assessed through the CV curves for these samples. Furthermore, for these samples, the low R_{ct} values are observed, signifying that the electronic charge transfer becomes easier in these samples due to the proper reduction of GO and the formation of optimally crystalline NG sheets. Now, comparing the EDL behavior among different sets of samples, it is clear that the sample prepared by using DMF as the solvent at 150 °C has the highest slope of the low-frequency tail (Figure 5e), and it shows the best rectangular CV curve (Figure 3e), very low R_{ct} , and the highest specific supercapacitance (Table 2).

3.3. XPS Study

The XPS spectra of the samples prepared using a particular solvent and at the optimum temperature, i.e., at 150 °C (THF), 180 °C (EtOH), 180 °C (ACN), 150 °C (water), 150 °C (DMF), 180 °C (EG), and 180 °C (NMP), for the solvents mentioned inside the brackets are shown in Figures 6 and 7.

Considering the N 1s spectra of all the samples shown in the left panel of Figure 6, we assign the peaks occurring at $\sim 398.3 \pm 0.3$ eV, 399.2 ± 0.3 eV, 400.1 ± 0.3 eV, 401.4 ± 0.3 eV, and 402.7 ± 0.3 eV to the pyridinic-N, amino-N, pyrrolic-N, graphitic-N, and oxidized-N species, respectively [2,45]. The fitting results (given in Table S4, ESI file) suggest that all types of N defects are present in all the samples but in different amounts. The middle panel of Figure 6 shows the C 1s spectrum of all the studied samples. The peaks occurring at 284.5 ± 0.3 eV, 285.3 ± 0.3 eV, 286.5 ± 0.3 eV, 287.6 ± 0.2 eV, and 289 ± 0.4 eV are assigned to the C=C aromatic/C-H bonds (sp^2), C-C aliphatic (sp^3), C-O-C/C-N bonds, and -C=O and O=C-OH/O=C-NH- bonds, respectively [46,47]. The fitting results are tabulated in Table S5 (ESI file). Similarly, the O 1s spectra of all our samples are shown in the right panel of Figure 6. The O 1s peaks are fitted to the following sub-peaks: quinone ($\sim 530.1 \pm 0.3$ eV), N-O (531.1 ± 0.3 eV), O=C-OH, (531.6 ± 0.3 eV),

-C=O (carbonyl oxygen, 532.3 ± 0.3 eV), C-O-C (533.1 ± 0.3 eV), C-OH (hydroxyl/phenolic oxygen, 534.01 ± 0.3 eV), and chemisorbed oxygen/adsorbed H_2O (535.32 ± 0.3 eV), respectively [2,48]. The O 1s peak of a particular oxygen species occurs almost at the same binding energy for all the samples, indicating that all the oxygenated groups are present within all samples with varying quantities. The fitting results are listed in Table S6 (ESI file). Considering the area under the C 1s, O 1s, and N 1s peaks of a particular sample, we have quantified the amount of C, O, and N present in our samples. The results are given in Table S7 (ESI file).

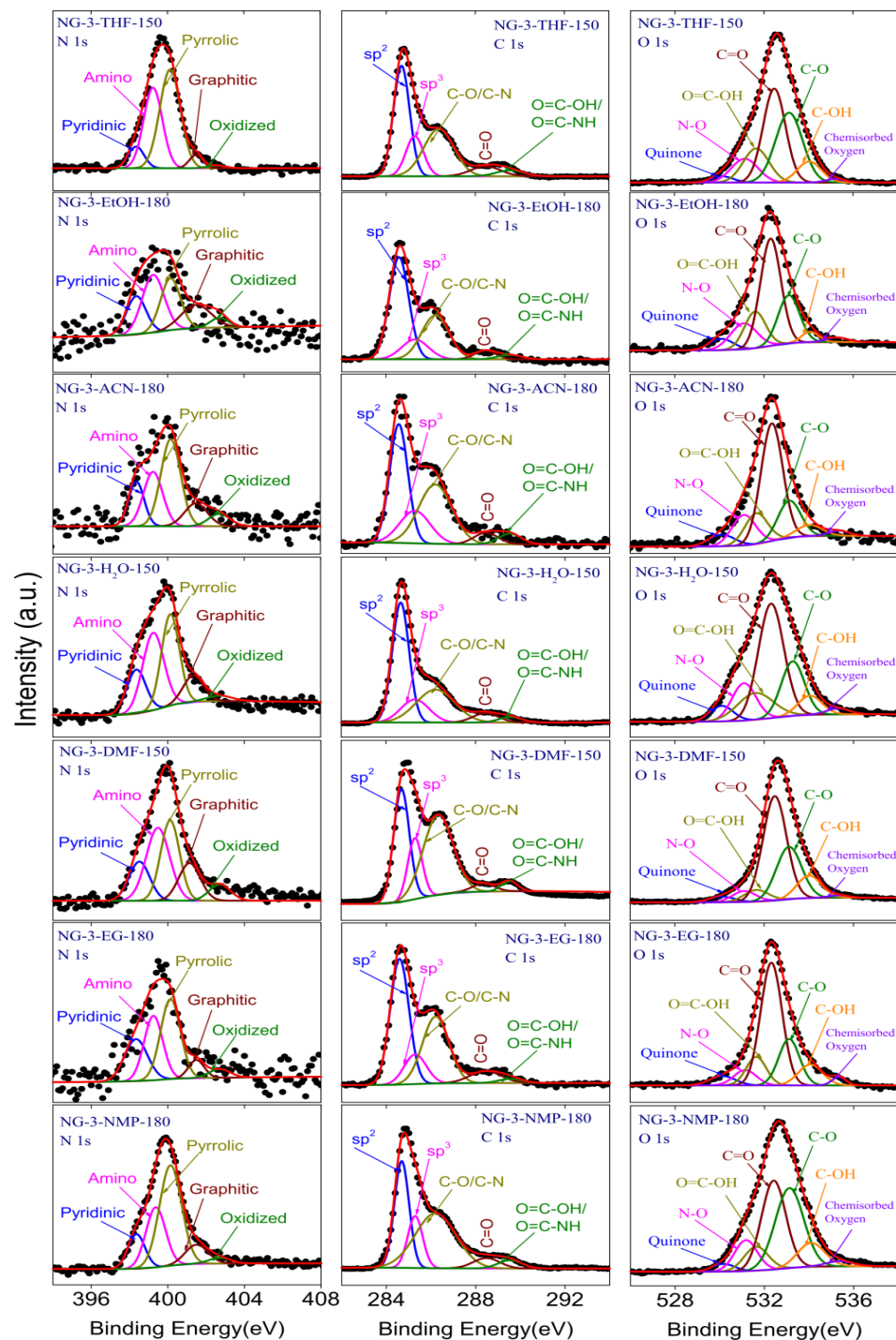


Figure 6. XPS spectra of synthesized NG-3 sample (left panel) N 1s, (middle panel) C 1s, and (right panel) O 1s.

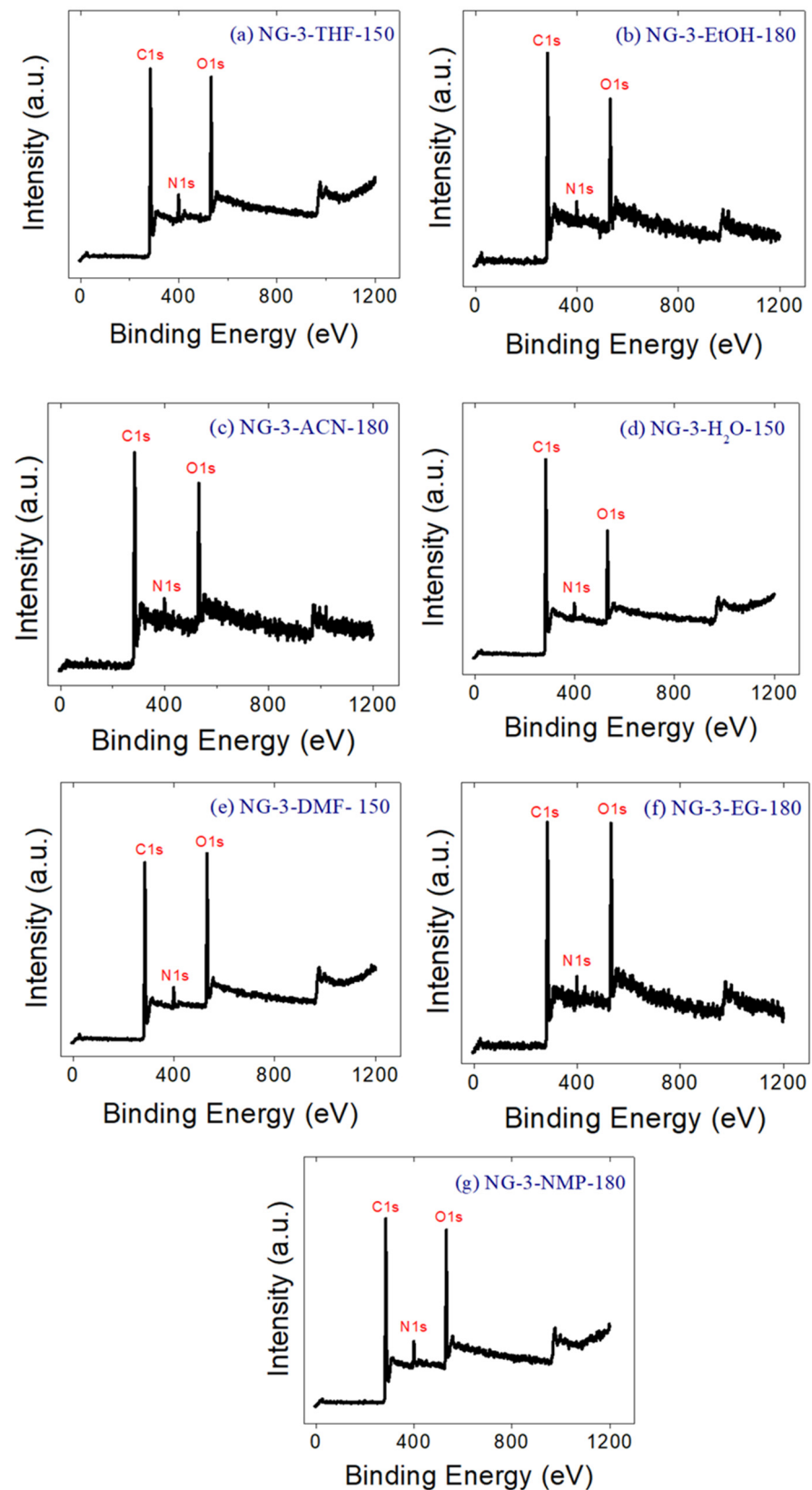


Figure 7. The wide XPS spectra of the synthesized samples in the full measured energy range.

To estimate the relative amount of N doping with respect to temperature, we have explored the XPS spectra obtained for a representative set of samples synthesized using DMF as the solvent and at three different synthesis temperatures, viz. 120 °C, 150 °C,

and 180 °C (Figure S9, ESI file). Furthermore, the reason for the disparity in the specific capacitance values of the samples synthesized using different solvents can be explained through the content and type of different N environments in different samples. The number of different types of N environments (in %) obtained from the fitting of these spectra are given in Table S8 (ESI file). The important information that can be revealed from this study is that the amount of graphitic N is more in the DMF-150 sample, which shows the highest supercapacitance (Table S4, ESI). As we have mentioned previously, this graphitic N could be the main reason for the high conductivity of the sample prepared using DMF at 150 °C. In contrast, for the NG-3-THF-150 sample, the percentage of graphitic nitrogen is significantly less (Table S4, ESI). Due to this, the sample may be less conductive and shows a substantially less specific capacitance of ~259 F/g at 0.5 A/g. The results illustrate that the presence of graphitic nitrogen in the NG-3-DMF-150 sample boosts its capacitive behavior, along with other structural and electronic parameters, as discussed previously. Furthermore, the high electronegativity of nitrogen assists in generating significant interactions with the solvated charged species coming to the surface of the NG electrode.

Furthermore, from Table S4 (ESI), it can be rationalized that an optimum amount of nitrogen doping is essential in maximizing the specific capacitance of the NG samples. If the N doping is too low, it may not modify the carbon framework suitably, and it may not show a high specific capacitance value. However, according to our results (Table S4, ESI), a moderate doping of nitrogen (~5.74%) is quite fruitful in achieving high C_{sp} , and this also provides the optimum crystallinity and structural stability to the graphenic framework of the sample. Maybe this amount of nitrogen doping is just enough to allow for a good permeation path and the effortless movement of electrons across the carbon framework during the charging and discharging of the supercapacitor. As the amount of nitrogen in the graphene sheets of the NG samples increases, too many defects are formed [49], resulting in breakage of the carbon frameworks, and the electron cloud is not well localized [50]. Hence, the control of N doping in NG samples is quite essential. To compare our results with the values reported in the literature, in Table S9 (ESI), we have listed the specific capacitances of different amounts of N doping in graphene-based materials synthesized using different methods. Clearly, all our optimized samples are either equivalent or better than the reported values (compare with Table 2), and among all our samples, the NG-3-DMF-150 sample shows an excellent C_{sp} value (~514 F/g). A two-electrode symmetric device had been demonstrated to show excellent cycling stability (~82% even after 8000 cycles) with this optimized material, as shown in our earlier work [33].

It is clear that the role of the dispersive solvents and the hydrothermal/solvothermal reaction temperature are important factors that decide the structural and electronic aspects of the NG sheets. These aspects control the supercapacitive behavior of the NG samples. Furthermore, as we have used 1 g of GO, the yield is higher than that reported in most of the literature; hence, the synthesis process is industrially scalable. Here, we try to explore the nature of the dispersive solvents responsible for the supercapacitive behavior of the NG sheets. As it is known, the dispersive solvents have their own intrinsic properties such as the boiling point, dipole moment, viscosity, dielectric constant, and dispersibility of GO in these solvents [51]. Hence, all these properties of the solvents play their vital roles in creating the differences in the structural and electronic properties of the NG samples, which in turn leads to the observed discrepancy in the trends of C_{sp} values. Furthermore, it is conceivable that a proper reduction of GO depends on these intrinsic properties. Among them, the viscosity of the solvent significantly influences the conductivity of the ions and the dispersibility of GO sheets in these liquids/gels. The dielectric constant (ϵ), along with the viscosity, are the two principal physical properties of the solvents that directly affect the ionic conductivity of the solvents. This is because the dissociation of the salts (such as urea in the present case, which dissociates into NH_3 and CO/CO_2) is associated with the dielectric constant, and the ionic/molecular mobility is elucidated by the viscosity of the solvents [39]. A low-viscosity solvent offers a superior conductance for the ions as compared to a highly viscous solvent. However, it does not frequently

happen, since viscosity is also related to the solvent's molecular interactions and dipole moment. These two features ascertain the dielectric constant (ϵ) of the solvent; a superior dielectric constant lessens ion coupling and ameliorates the conductivity of a known salt. Therefore, even though lower viscosity ameliorates the real mobility of the free ions, the small dielectric constant, which is generally coupled with low-viscosity solvents (due to feeble intermolecular interactions), leans to abridge the conductivity [39].

The dispersibility of GO in various solvents has been studied by several researchers, where they demonstrated that as-synthesized GO dispersions in organic solvents (THF, ethanol, acetonitrile, ethylene glycol, and NMP) were noticed to display short-term colloidal constancy compared to the dispersion of the similar materials in water and DMF [51]. Several studies examined that ethylene glycol and THF dispersions acquired a fairly superior quantity of precipitate compared to water, DMF, and NMP dispersions, signifying that the other solvents acquire a moderately lower dispersion capability. Water exhibits the most superior dispersion capability, as it delivers the utmost absorption and consequently the prevalent amount of suspended GO, pursued narrowly by DMF and NMP [26]. Ethylene glycol and THF demonstrate extremely analogous dispersion skills toward as-synthesized GO, even though they are evidently lighter compared to other solvents [27]. Several researchers observed that as-synthesized GO nanoplatelets are showing more dispersibility in *N,N*-dimethylformamide (DMF) devoid of chemical modification [52,53].

Presently, the mechanisms that permit the steady dispersion of GO in the discussed organic solvents are unambiguous. An essential but insufficient circumstance appears to be that the solvent molecules should be noticeably polar. This is sensible, as the GO sheets are noticeably and profoundly ornamented by polar oxygen-containing functional groups (hydroxyl, carbonyl, and carboxyl), which is the main cause to endorse a fine GO sheet-solvent interaction. It is known that water and four other organic solvents demonstrate noteworthy electrical dipole moment values as follows: 1.85 D (water), 3.25 D (DMF), 3.75 D (NMP), 1.75 D (THF), and 2.31 D (ethylene glycol). On the contrary, the solvents having a minute dipole moment (*n*-hexane, 0.085 D; *o*-xylene, 0.45 D) are evidently unable to disperse the as-synthesized GO sheets. Conversely, there are a variety of solvents with elevated dipole moments (mainly DMSO, 4.09 D) that are unsuccessful in affording GO dispersions with long-lasting dispersion constancy, which advocates that additional features excluding solvent polarity are imperative for examining superior dispersibility [40,41].

Hence, from the above observations, we concluded that the role of the solvents and temperature is very important for the synthesis of nitrogen-doped reduced graphene oxide materials for achieving high supercapacitance. Furthermore, it is clear that all the different physical properties (such as the boiling point, dipole moment, viscosity, dielectric constant, and dispersibility of GO) of the solvents, along with the synthesis temperature, are significant in describing the discrepancy in specific supercapacitance values observed for the synthesized samples at different temperatures in various solvents. Overall, DMF is an ideal solvent for the proper reduction of GO and for the perfect stacking of NG sheets.

4. Conclusions

We have used different solvents such as THF, ethanol, acetonitrile, H₂O, DMF, ethylene glycol, and NMP for the solvothermal synthesis of N-doped reduced graphene oxide (NG) at different synthesis temperatures between 60 °C and 195 °C. Our results show that in these solvents, GO is differently reduced and differently exfoliated into individual flakes of a few layers of N-doped reduced graphene oxide-like sheets with lateral dimensions of a few nanometers. The suitable conditions for the reduction and simultaneous N doping in the reduced GO sheets, along with proper stacking of the NG sheets, are identified in several organic/aqueous solvents. Our results demonstrated that among all solvents, the NG sample prepared using DMF exhibits the best supercapacitive performance (with a specific capacitance of 514 F/g at 0.5 A/g). Moreover, the appropriate stacking of the NG sheets is achieved with an optimum number of defects required for appreciably high conductivity in comparison to the other solvents. This supercapacitance value is the highest

among all our samples and also a competitive value among all the known state-of-the-art lightweight materials. Hence, our results reveal the optimum synthesis conditions and suitable solvent parameters required for the synthesis of high-quality NG sheets showing excellent supercapacitor performance for their direct use in industrial applications.

Supplementary Materials: The following supporting information can be downloaded at: <https://www.mdpi.com/article/10.3390/c10040089/s1>. References [54–60] are cited in the supplementary materials.

Author Contributions: A.Y.: conceptualization, physical and electrochemical measurements, data analysis, writing—original draft, writing—review and editing. R.K.: conceptualization, writing—review and editing. D.J.—data analysis, writing—review and editing. N.T.—data analysis, writing—review and editing. F.Y.—writing—review and editing, project funding acquisition. B.S.: project administration, project funding acquisition, data analysis, writing—review and editing. All authors have read and agreed to the published version of the manuscript.

Funding: The funding for this work was received from the ISRO-IISc STC (project code- ISTC/CMR/BS/431) and the U.S. National Science Foundation (NSF) under grant #DMR-2122044 and the U.S. Army Research Office (ARO) under grant #W911NF2210109.

Data Availability Statement: The raw/processed data required to reproduce these findings cannot be shared at this time as the data also form part of an ongoing study.

Acknowledgments: The authors acknowledge SSCU, IPC, AFMM and CeNSE-MNCF at IISc Bengaluru for using the characterization facilities.

Conflicts of Interest: There are no conflicts of interest.

References

- Wang, Z.F.; Tang, C.; Sun, Q.; Han, Y.L.; Wang, Z.J.; Xie, L.; Zhang, S.C.; Su, F.Y.; Chen, C.M. Effect of N-Doping-Derived Solvent Adsorption on Electrochemical Double Layer Structure and Performance of Porous Carbon. *J. Energy Chem.* **2023**, *80*, 120–127. [CrossRef]
- Ajraivat, K.; Pandey, O.P.; Brar, L.K. Significance of N Bonding Configurations in N-Doped Graphene for Enhanced Supercapacitive Performance: A Comparative Study in Aqueous Electrolytes. *FlatChem* **2024**, *43*, 100588. [CrossRef]
- Li, X.; Cao, J.; Chen, J.; Zhu, Y.; Xia, H.; Xu, Z.; Gu, C.; Xie, J.; Jones, M.; Lyu, C.; et al. UV-Induced Synthesis of Graphene Supported Iridium Catalyst with Multiple Active Sites. *Adv. Func. Mater.* **2024**, *34*, 2313530. [CrossRef]
- Fan, Y.F.; Yi, Z.L.; Song, G.; Wang, Z.F.; Chen, C.J.; Xie, L.J.; Sun, G.H.; Su, F.Y.; Chen, C.M. Self-Standing Graphitized Hybrid Nanocarbon Electrodes towards High-Frequency Supercapacitors. *Carbon* **2021**, *185*, 630–640. [CrossRef]
- Wang, H.; Maiyalagan, T.; Wang, X. Review on Recent Progress in Nitrogen-Doped Graphene: Synthesis, Characterization, and Its Potential Applications. *ACS Catal.* **2012**, *2*, 781–794. [CrossRef]
- Lu, Y.; Huang, Y.; Zhang, M.; Chen, Y. Nitrogen-Doped Graphene Materials for Supercapacitor Applications. *J. Nanosci. Nanotechnol.* **2014**, *14*, 1134–1144. [CrossRef]
- Jing, M.; Wu, T.; Zhou, Y.; Li, X.; Liu, Y. Nitrogen-Doped Graphene via In-Situ Alternating Voltage Electrochemical Exfoliation for Supercapacitor Application. *Front. Chem.* **2020**, *8*, 428. [CrossRef]
- Nolan, H.; Mendoza-Sanchez, B.; Ashok Kumar, N.; McEvoy, N.; O'Brien, S.; Nicolosi, V.; Duesberg, G.S. Nitrogen-Doped Reduced Graphene Oxide Electrodes for Electrochemical Supercapacitors. *Phys. Chem. Chem. Phys.* **2014**, *16*, 2280–2284. [CrossRef]
- Deng, D.; Pan, X.; Yu, L.; Cui, Y.; Jiang, Y.; Qi, J.; Li, W.X.; Fu, Q.; Ma, X.; Xue, Q.; et al. Toward N-Doped Graphene via Solvothermal Synthesis. *Chem. Mater.* **2011**, *23*, 1188–1193. [CrossRef]
- Jeong, H.M.; Lee, J.W.; Shin, W.H.; Choi, Y.J.; Shin, H.J.; Kang, J.K.; Choi, J.W. Nitrogen-Doped Graphene for High-Performance Ultracapacitors and the Importance of Nitrogen-Doped Sites at Basal Planes. *Nano Lett.* **2011**, *11*, 2472–2477. [CrossRef]
- Qu, L.; Liu, Y.; Baek, J.-B.; Dai, L. Nitrogen-Doped Reduced-Graphene Oxide as an Efficient Metal-Free Electrocatalyst for Oxygen Reduction in Fuel Cells. *ACS Nano* **2010**, *4*, 1321–1326. [CrossRef] [PubMed]
- Wang, Y.; Shao, Y.; Matson, D.W.; Li, J.; Lin, Y. Nitrogen-Doped Graphene and Its Application in Electrochemical Biosensing. *ACS Nano* **2010**, *4*, 1790–1798. [CrossRef] [PubMed]
- Yadav, A.; Kumar, R.; Yadav, K.; Thomas, N.; Mishra, M.; Sahoo, B. Synthesis, Characterization and Insights into the Supercapacitive and Electrocatalytic (OER) Bi-Functional Properties of Nitrogen-Doped Reduced Graphene Oxide Using Dicyandiamide Precursor. *Solid State Sci.* **2024**, *147*, 107377. [CrossRef]
- Hasan, S.A.; Tsekoura, E.K.; Sternhagen, V.; Strømme, M. Evolution of the Composition and Suspension Performance of Nitrogen-Doped Graphene. *J. Phys. Chem. C* **2012**, *116*, 6530–6536. [CrossRef]
- Fan, X.; Yu, C.; Yang, J.; Ling, Z.; Qiu, J. Hydrothermal Synthesis and Activation of Composite for High-Performance Supercapacitors. *Carbon* **2014**, *70*, 130–141. [CrossRef]

16. Lee, J.W.; Ko, J.M.; Kim, J.D. Hydrothermal Preparation of Nitrogen-Doped Graphene Sheets via Hexamethylenetetramine for Application as Supercapacitor Electrodes. *Electrochim. Acta* **2012**, *85*, 459–466. [\[CrossRef\]](#)
17. Zhao, Y.; Hu, C.; Hu, Y.; Cheng, H.; Shi, G.; Qu, L. A Versatile, Ultralight, Nitrogen-Doped Graphene Framework. *Angew. Chem. Int. Ed.* **2012**, *51*, 11371–11375. [\[CrossRef\]](#)
18. Wang, D.; Min, Y.; Yu, Y.; Peng, B. A General Approach for Fabrication of Nitrogen-Doped Graphene Sheets and Its Application in Supercapacitors. *J. Colloid Interface Sci.* **2014**, *417*, 270–277. [\[CrossRef\]](#)
19. Lei, Z.; Lu, L.; Zhao, X.S. The Electrocapacitive Properties of Graphene Oxide Reduced by Urea. *Energy Environ. Sci.* **2012**, *5*, 6391–6399. [\[CrossRef\]](#)
20. Lee, Y.H.; Chang, K.H.; Hu, C.C. Differentiate the Pseudocapacitance and Double-Layer Capacitance Contributions for Nitrogen-Doped Reduced Graphene Oxide in Acidic and Alkaline Electrolytes. *J. Power Sources* **2013**, *227*, 300–308. [\[CrossRef\]](#)
21. Wang, T.; Wang, L.; Wu, D.; Xia, W.; Zhao, H.; Jia, D. Hydrothermal Synthesis of Nitrogen-Doped Graphene Hydrogels Using Amino Acids with Different Acidities as Doping Agents. *J. Mater. Chem. A* **2014**, *2*, 8352–8361. [\[CrossRef\]](#)
22. Long, D.; Li, W.; Ling, L.; Miyawaki, J.; Mochida, I.; Yoon, S.H. Preparation of Nitrogen-Doped Graphene Sheets by a Combined Chemical and Hydrothermal Reduction of Graphene Oxide. *Langmuir* **2010**, *26*, 16096–16102. [\[CrossRef\]](#) [\[PubMed\]](#)
23. Sun, L.; Wang, L.; Tian, C.; Tan, T.; Xie, Y.; Shi, K.; Li, M.; Fu, H. Nitrogen-Doped Graphene with High Nitrogen Level via a One-Step Hydrothermal Reaction of Graphene Oxide with Urea for Superior Capacitive Energy Storage. *RSC Adv.* **2012**, *2*, 4498–4506. [\[CrossRef\]](#)
24. Śliwak, A.; Grzyb, B.; Diez, N.; Gryglewicz, G. Nitrogen-Doped Reduced Graphene Oxide as Electrode Material for High Rate Supercapacitors. *Appl. Surf. Sci.* **2017**, *399*, 265–271. [\[CrossRef\]](#)
25. Lai, L.; Chen, L.; Zhan, D.; Sun, L.; Liu, J.; Lim, S.H.; Poh, C.K.; Shen, Z.; Lin, J. One-Step Synthesis of NH₂-Graphene from in Situ Graphene-Oxide Reduction and Its Improved Electrochemical Properties. *Carbon* **2011**, *49*, 3250–3257. [\[CrossRef\]](#)
26. Paredes, J.I.; Villar-Rodil, S.; Martínez-Alonso, A.; Tascón, J.M.D. Graphene Oxide Dispersions in Organic Solvents. *Langmuir* **2008**, *24*, 10560–10564. [\[CrossRef\]](#)
27. Park, S.; An, J.; Jung, I.; Piner, R.D.; An, S.J.; Li, X.; Velamakanni, A.; Ruoff, R.S. Colloidal Suspensions of Highly Reduced Graphene Oxide in a Wide Variety of Organic Solvents. *Nano Lett.* **2009**, *9*, 1593–1597. [\[CrossRef\]](#)
28. Hernandez, Y.; Lotya, M.; Rickard, D.; Bergin, S.D.; Coleman, J.N. Measurement of Multicomponent Solubility Parameters for Graphene Facilitates Solvent Discovery. *Langmuir* **2010**, *26*, 3208–3213. [\[CrossRef\]](#)
29. Gopalakrishnan, K.; Moses, K.; Govindaraj, A.; Rao, C.N.R. Supercapacitors Based on Nitrogen-Doped Reduced Graphene Oxide and Borocarbonitrides. *Solid State Commun.* **2013**, *175–176*, 43–50. [\[CrossRef\]](#)
30. Jiang, B.; Tian, C.; Wang, L.; Sun, L.; Chen, C.; Nong, X.; Qiao, Y.; Fu, H. Highly Concentrated, Stable Nitrogen-Doped Graphene for Supercapacitors: Simultaneous Doping and Reduction. *Appl. Surf. Sci.* **2012**, *258*, 3438–3443. [\[CrossRef\]](#)
31. Mayyas, M.; Li, H.; Kumar, P.; Ghasemian, M.B.; Yang, J.; Wang, Y.; Lawes, D.J.; Han, J.; Saborio, M.G.; Tang, J.; et al. Liquid-Metal-Templated Synthesis of 2D Graphitic Materials at Room Temperature. *Adv. Mater.* **2020**, *32*, 2001997. [\[CrossRef\]](#) [\[PubMed\]](#)
32. Liu, X.; Lyu, D.; Merlet, C.; Leesmith, M.J.A.; Hua, X.; Xu, Z.; Grey, C.P.; Forse, A.C. Structural Disorder Determines Capacitance in Nanoporous Carbons. *Science* **2024**, *384*, 321–325. [\[CrossRef\]](#) [\[PubMed\]](#)
33. Yadav, A.; Kumar, R.; Sahoo, B. Exploring Supercapacitance of Solvothermally Synthesized N-RGO Sheet: Role of N-Doping and the Insight Mechanism. *Phys. Chem. Chem. Phys.* **2022**, *24*, 1059–1071. [\[CrossRef\]](#) [\[PubMed\]](#)
34. Marcano, D.C.; Kosynkin, D.V.; Berlin, J.M.; Sinitskii, A.; Sun, Z.; Slesarev, A.; Alemany, L.B.; Lu, W.; Tour, J.M. Improved Synthesis of Graphene Oxide. *ACS Nano* **2010**, *4*, 4806–4814. [\[CrossRef\]](#)
35. Yadav, A.; Kumar, R.; Kumar, S.; Sahoo, B. Mechanistic Insights into the Roles of Precursor Content, Synthesis Time, and Dispersive Solvent in Maximizing Supercapacitance of N-RGO Sheets. *J. Alloys Compd.* **2024**, *971*, 172648. [\[CrossRef\]](#)
36. Saraf, M.; Natarajan, K.; Mobin, S.M.; Natarajan, K.; Mobin, S.M. Robust Nanocomposite of Nitrogen-Doped Reduced Graphene Oxide and MnO₂ Nanorods for High-Performance Supercapacitors and Nonenzymatic Peroxide Sensors. *ACS Sustain. Chem. Eng.* **2018**, *6*, 10489–10504. [\[CrossRef\]](#)
37. Sun, Q.; Yi, Z.; Fan, Y.; Xie, L.; Wang, Z.; Sun, G.; Wang, Z.; Huang, X.; Liu, Z.; Su, F.; et al. Whole Landscape of the Origin and Evolution of Gassing in Supercapacitors at a High Voltage. *ACS Appl. Mater. Interfaces* **2023**, *15*, 54386. [\[CrossRef\]](#)
38. Chen, W.; Yan, L. Preparation of Graphene by a Low-Temperature Thermal Reduction at Atmosphere Pressure. *Nanoscale* **2010**, *2*, 559–563. [\[CrossRef\]](#)
39. Pal, B.; Yang, S.; Ramesh, S.; Thangadurai, V.; Jose, R. Electrolyte Selection for Supercapacitive Devices: A Critical Review. *Nanoscale Adv.* **2019**, *1*, 3807–3835. [\[CrossRef\]](#)
40. Furtado, C.A.; Kim, U.J.; Gutierrez, H.R.; Pan, L.; Dickey, E.C.; Eklund, P.C. Debundling and Dissolution of Single-Walled Carbon Nanotubes in Amide Solvents. *J. Am. Chem. Soc.* **2004**, *126*, 6095–6105. [\[CrossRef\]](#)
41. Ausman, K.D.; Piner, R.; Lourie, O.; Ruoff, R.S.; Korobov, M. Organic Solvent Dispersions of Single-Walled Carbon Nanotubes: Toward Solutions of Pristine Nanotubes. *J. Phys. Chem. B* **2000**, *104*, 8911–8915. [\[CrossRef\]](#)
42. Li, X.; Zang, X.; Li, Z.; Li, X.; Li, P.; Sun, P.; Lee, X. Large-Area Flexible Core-Shell Graphene / Porous Carbon Woven Fabric Films for Fiber Supercapacitor Electrodes. *Adv. Func. Mater.* **2013**, *23*, 4862–4869. [\[CrossRef\]](#)
43. Qu, D. Studies of the Activated Mesocarbon Microbeads Used in Double-Layer Supercapacitors. *J. Power Sources* **2002**, *109*, 403–411. [\[CrossRef\]](#)

44. Chen, W.-C.; Wen, T.-C.; Teng, H. Polyaniline-Deposited Porous Carbon Electrode for Supercapacitor. *Electrochim. Acta* **2003**, *48*, 641–649. [\[CrossRef\]](#)
45. Mandal, B.; Saha, S.; Das, D.; Panda, J.; Das, S.; Sarkar, R.; Tudu, B. Supercapacitor Performance of Nitrogen Doped Graphene Synthesized via DMF Assisted Single-Step Solvothermal Method. *FlatChem* **2022**, *34*, 100400. [\[CrossRef\]](#)
46. Ajravat, K.; Rajput, S.; Brar, L.K. Microwave Assisted Hydrothermal Synthesis of N Doped Graphene for Supercapacitor Applications. *Diam. Relat. Mater.* **2022**, *129*, 109373. [\[CrossRef\]](#)
47. Sobaszek, M.; Brzhezinskaya, M.; Olejnik, A.; Mortet, V.; Alam, M.; Sawczak, M.; Ficek, M.; Gazda, M.; Weiss, Z.; Bogdanowicz, R. Highly Occupied Surface States at Deuterium-Grown Boron-Doped Diamond Interfaces for Efficient Photoelectrochemistry. *Small* **2023**, *19*, 2208265. [\[CrossRef\]](#)
48. Brzhezinskaya, M.; Mishakov, I.V.; Bauman, Y.I.; Shubin, Y.V.; Maksimova, T.A.; Stoyanovskii, V.O.; Gerasimov, E.Y.; Vedyagin, A.A. One-Pot Functionalization of Catalytically Derived Carbon Nanostructures with Heteroatoms for Toxic-Free Environment. *Appl. Surf. Sci.* **2022**, *590*, 153055. [\[CrossRef\]](#)
49. Wang, M.; Duong, L.D.; Mai, N.T.; Kim, S.; Kim, Y.; Seo, H.; Kim, Y.C.; Jang, W.; Lee, Y.; Suhr, J.; et al. All-Solid-State Reduced Graphene Oxide Supercapacitor with Large Volumetric Capacitance and Ultralong Stability Prepared by Electrophoretic Deposition Method. *ACS Appl. Mater. Interfaces* **2015**, *7*, 1348–1354. [\[CrossRef\]](#)
50. Kumar, M.P.; Kesavan, T.; Kalita, G.; Ragupathy, P.; Narayanan, T.N.; Pattanayak, D.K. On the Large Capacitance of Nitrogen Doped Graphene Derived by a Facile Route. *RSC Adv.* **2014**, *4*, 38689–38697. [\[CrossRef\]](#)
51. Konios, D.; Stylianakis, M.M.; Stratakis, E.; Kymakis, E. Dispersion Behaviour of Graphene Oxide and Reduced Graphene Oxide. *J. Colloid Interface Sci.* **2014**, *430*, 108–112. [\[CrossRef\]](#) [\[PubMed\]](#)
52. Cai, D.; Song, M.; Xu, C. Highly Conductive Carbon-Nanotube/Graphite-Oxide Hybrid Films. *Adv. Mater.* **2008**, *20*, 1706–1709. [\[CrossRef\]](#)
53. Cai, D.; Song, M. Preparation of Fully Exfoliated Graphite Oxide Nanoplatelets in Organic Solvents. *J. Mater. Chem.* **2007**, *17*, 3678–3680. [\[CrossRef\]](#)
54. Pawlyta, M.; Rouzaud, J.N.; Duber, S. Raman Microspectroscopy Characterization of Carbon Blacks: Spectral Analysis and Structural Information. *Carbon* **2015**, *84*, 479–490. [\[CrossRef\]](#)
55. Cañado, L.G.; Takai, K.; Enoki, T.; Endo, M.; Kim, Y.A.; Mizusaki, H.; Jorio, A.; Coelho, L.N.; Magalhães-Paniago, R.; Pimenta, M.A. General Equation for the Determination of the Crystallite Size L_a of Nanographite by Raman Spectroscopy. *Appl. Phys. Lett.* **2006**, *88*, 163106. [\[CrossRef\]](#)
56. Hassan, F.M.; Chabot, V.; Li, J.; Kim, B.K.; Ricardez-Sandoval, L.; Yu, A. Pyrrolic-Structure Enriched Nitrogen Doped Graphene for Highly Efficient next Generation Supercapacitors. *J. Mater. Chem. A* **2013**, *1*, 2904–2912. [\[CrossRef\]](#)
57. Wang, C.; Zhou, Y.; Sun, L.; Zhao, Q.; Zhang, X.; Wan, P.; Qiu, J. N/P-Codoped Thermally Reduced Graphene for High-Performance Supercapacitor Applications. *J. Phys. Chem. C* **2013**, *117*, 14912–14919. [\[CrossRef\]](#)
58. Wang, P.; He, H.; Xu, X.; Jin, Y. Significantly Enhancing Supercapacitive Performance of Nitrogen-Doped Graphene Nanosheet Electrodes by Phosphoric Acid Activation. *ACS Appl. Mater. Interfaces* **2014**, *6*, 1563–1568. [\[CrossRef\]](#)
59. Lu, Y.; Zhang, F.; Zhang, T.; Leng, K.; Zhang, L.; Yang, X.; Ma, Y.; Huang, Y.; Zhang, M.; Chen, Y. Synthesis and Supercapacitor Performance Studies of N-Doped Graphene Materials Using o-Phenylenediamine as the Double-N Precursor. *Carbon* **2013**, *63*, 508–516. [\[CrossRef\]](#)
60. Wen, Z.; Wang, X.; Mao, S.; Bo, Z.; Kim, H.; Cui, S.; Lu, G.; Feng, X.; Chen, J. Crumpled Nitrogen-Doped Graphene Nanosheets with Ultrahigh Pore Volume for High-Performance Supercapacitor. *Adv. Mater.* **2012**, *24*, 5610–5616. [\[CrossRef\]](#)

Disclaimer/Publisher's Note: The statements, opinions and data contained in all publications are solely those of the individual author(s) and contributor(s) and not of MDPI and/or the editor(s). MDPI and/or the editor(s) disclaim responsibility for any injury to people or property resulting from any ideas, methods, instructions or products referred to in the content.